Chapter-4

Structural and magnetic properties of $Ni_{1-x}Zn_xFe_2O_4$ nano-powders synthesized by oxalate based precursor method

4.1 Introduction

Synthesis of nanoparticulated spinel ferrite exhibits unpredictable physical and chemical properties, which are entirely different from those of usual bulk materials, because of extremely small grain size or large specific surface area. Therefore synthesis and characterization of the nanocrystalline spinel ferrite powders have attracted increasing attention recently [1, 2].

$Ni_{1-x}Zn_xFe_2O_4$ is a well-known spinel magnetic material. In the inverse spinel structure of $NiFe_2O_4$, the tetrahedral sites are occupied by ferric ions and octahedral, by ferric and nickel ions. $Ni_{1-x}Zn_xFe_2O_4$ ferrites are ferrimagnetic materials with a large number of technological applications in telecommunications and entertainment electronics. Ni-Zn ferrites are among the most widely used soft magnetic materials because of high frequency applications as they posses high electrical resistivity and low eddy current losses [3-5]. It is known that magnetic properties of ferrites are sensitive to preparation techniques, their microstructures and especially to grain size [6]. The electrical and magnetic properties of such ferrites depend strongly on the distribution of cations at the tetrahedral (A) and the octahedral [B] sites in the lattice [7,8]. It is well known that zinc ions can be used to alter the saturation magnetization. It is believed that the addition of zinc ions also affects the lattice parameter and it would therefore be expected to change the Curie temperature of the material [9]. The substitution of divalent ions in pure ferrites leads to the modification of the structural, electrical and magnetic properties [10]. The conventional solid-state reaction route is widely used for the production of ferrite because of its low cost and suitability for large scale production. The oxalate based precursor method is used to speed up the synthesis of complex materials.

It is a simple process, which offers a significant saving in time and energy consumption over the traditional methods.

Several researchers have reported the synthesis of $Ni_{1-x}Zn_xFe_2O_4$ using different techniques like, refluxing process, ceramic, hydrothermal [11], combustion [12], coprecipitation [13], reverse micelle process [14], spark plasma sintering [15], citrate precursor [16], micro emulsion [17], ball milling [18], hydrothermal [19] etc.

In this work, we present the results of systematic doping of non-magnetic Zn content on the structural and magnetic properties of nanocrystalline $Ni_{1-x}Zn_xFe_2O_4$ synthesized by oxalic acid based precursor method.

4.2 Experimental procedures

4.2.1 Synthesis of $Ni_{1-x}Zn_xFe_2O_4$ (x = 0.0, 0.2, 0.4, 0.6, 0.8) nanopowders.

Nanocrystalline powders of $Ni_{1-x}Zn_xFe_2O_4$ (x =0.0, 0.2, 0.4, 0.6, 0.8) were synthesized by oxalic acid based precursor method [20, 21]. All of the chemicals were analytical grade from Sigma–Aldrich with purity ≥ 99% and were used without any further purification. In a typical procedure, the nickel nitrate hydrate Ni $(NO_3)_2 \cdot 6H_2O$, zinc nitrate hydrate $Zn(NO_3)_2 \cdot 6H_2O$, ferric nitrate nonahydrate $Fe(NO_3)_3 \cdot 9H_2O$ were used as starting materials. Stoichiometric amounts of metal nitrates were dissolved in deionized water to get clear solution. The obtained aqueous solution of metal nitrates was mixed with oxalic acid in a molar ratio ranging from 1:3 to 1:0.15. The mixture solution were moved on to magnetic stirrer and stirred for 2hr at room temperature. The reaction mixtures turned turbid by varying molar ratios 1:3 and 1:2. When the molar ratio was further lowered to 1:1, precursor solution showed different colour shades. The resultant mixtures were evaporated on a hot plate at 150^0C for 2hr.

The obtained raw powders were thermally heat treated at 300^0C for 4hr to get the single phase nanocrystalline spinel structure.

4.2.2 Characterization of $Ni_{1-x}Zn_xFe_2O_4$ (x = 0.0, 0.2, 0.4, 0.6, 0.8) nanopowders

The structural characterization of the prepared Ni-Zn ferrite nanopowders was carried out using Philips X-ray diffraction system with Ni filter using Cu –Kα radiation (wave length λ= 1.54 A^o). The average particle size *D* was calculated using most intense peak (311) employing the Scherer formula. The particle size and morphology was carried out using FE-SEM (model JSM-7000F) manufactured by JEOL Ltd. The FE-SEM was linked to an EDS/INCA 350 (energy dispersive X-ray analyzer) manufactured by Oxford Instruments Ltd. The structural changes with calcination temperature are observed by ABB Bomem MB 102 infrared spectrometer equipped with CsI optics and DTGS detector. The samples were mixed with KBr and made in the form of pellets and recorded at 4 cm^{-1} resolution (10 consecutive scans were averaged for each spectrum), giving the spectra in the 4000 - 200 cm^{-1} range. Magnetic measurements were performed using Lakeshore VSM 7410. Magnetic hysteresis loops were measured at room temperature with maximal applied magnetic fields of 10 kOe. Maximum magnetization, coercivity and remanent magnetization were observed from the hysteresis loops.

4.3 Results and discussions

4.3.1 Structural characterization

Figure 4.1 shows the X-ray diffractograms of $Ni_{1-x}Zn_xFe_2O_4$ (x = 0.0, 0.2, 0.4, 0.6, 0.8, 1.0). The XRD patterns clearly indicate that the prepared samples contain cubic spinel structure only. From the XRD it can be clearly seen that no secondary phases exists and the prepared ferrite nanopowders contains only single phase spinel structure. A close examination of XRD patterns as shown in Figure 4.2 reveals that the diffraction peaks became broader with increasing Zn content x, which may be attributed to the reduced nanocrystallite size with Zn doping. It can be clearly observed from Figure 4.2 that the full-width at half maximum (FWHM) increases upon increasing Zn doping and it resulted in the decrease of the particle size. The probable reason for this kind effect may be due to the reaction time and temperature during the synthesis process. Generally in the case of nano ferrites, behavior such as decrease in the particle with the increase in the doping concentration is seen quite common [22, 23]. The sizes of crystallite size of all the samples is evaluated by measuring the FWHM (Figure 4.2) of the most intense peak (311) using the Scherer formula (equation 4.1).

$$D = \frac{0.9\lambda}{\beta \cos\theta} \tag{4.1}$$

where, D is the average crystalline size, λ is the X-ray wavelength used, β is the angular line width of half maximum intensity and θ is the Bragg angle in degrees.

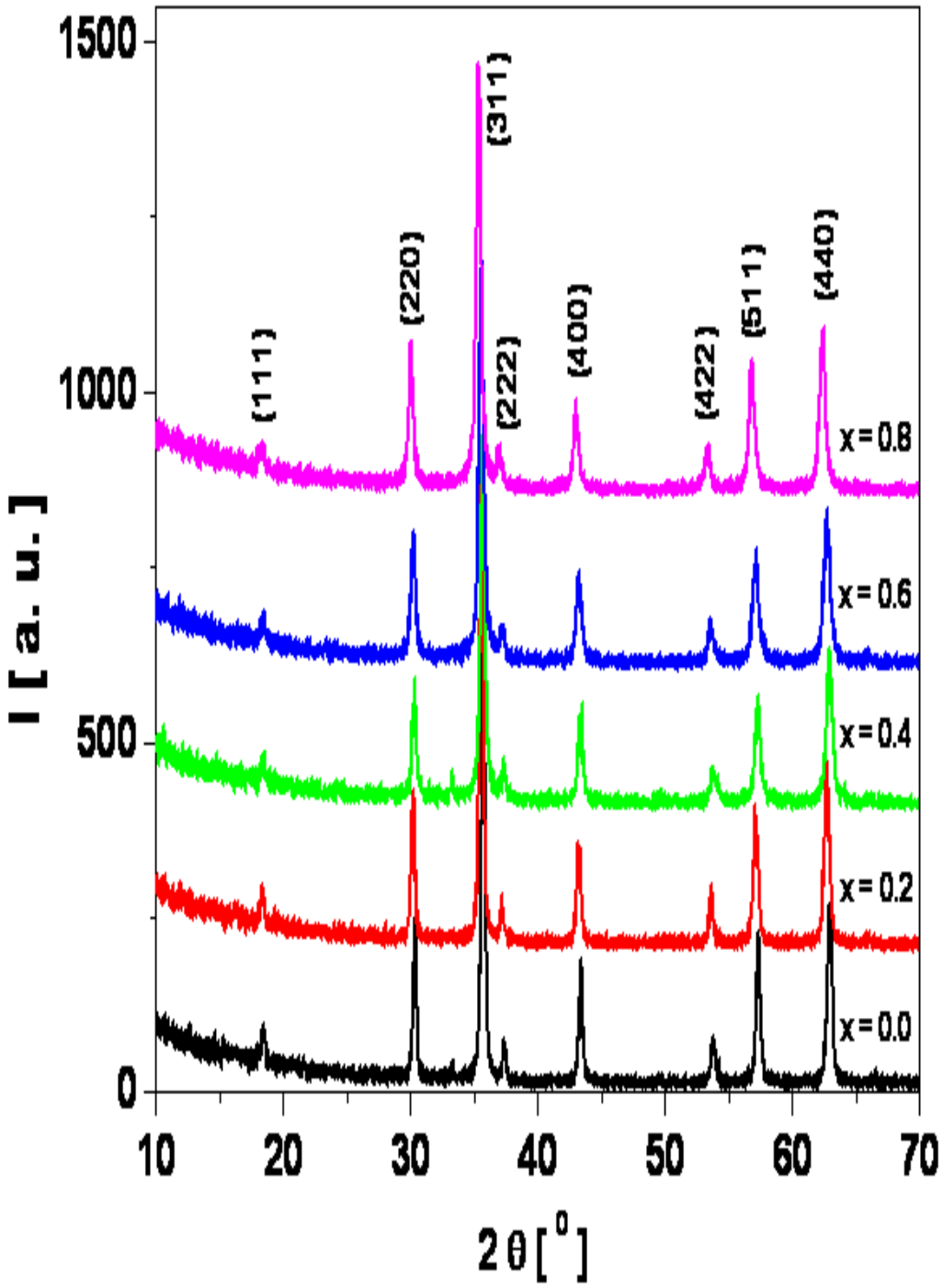

Figure 4.1: X-ray diffraction pattern of $Ni_{1-x}Zn_xFe_2O_4$ (x = 0.0, 0.2, 0.4, 0.6, and 0.8) nanoparticles.

The observed particle size of $Ni_{1-x}Zn_xFe_2O_4$ (x = 0.0, 0.2, 0.4, 0.6, 0.8) are listed in Table 4.1. Furthermore, it is observed from Table 4.1 that, the particle size D decreases with increasing Zn content x and is plotted as shown in the Figure 4.3.

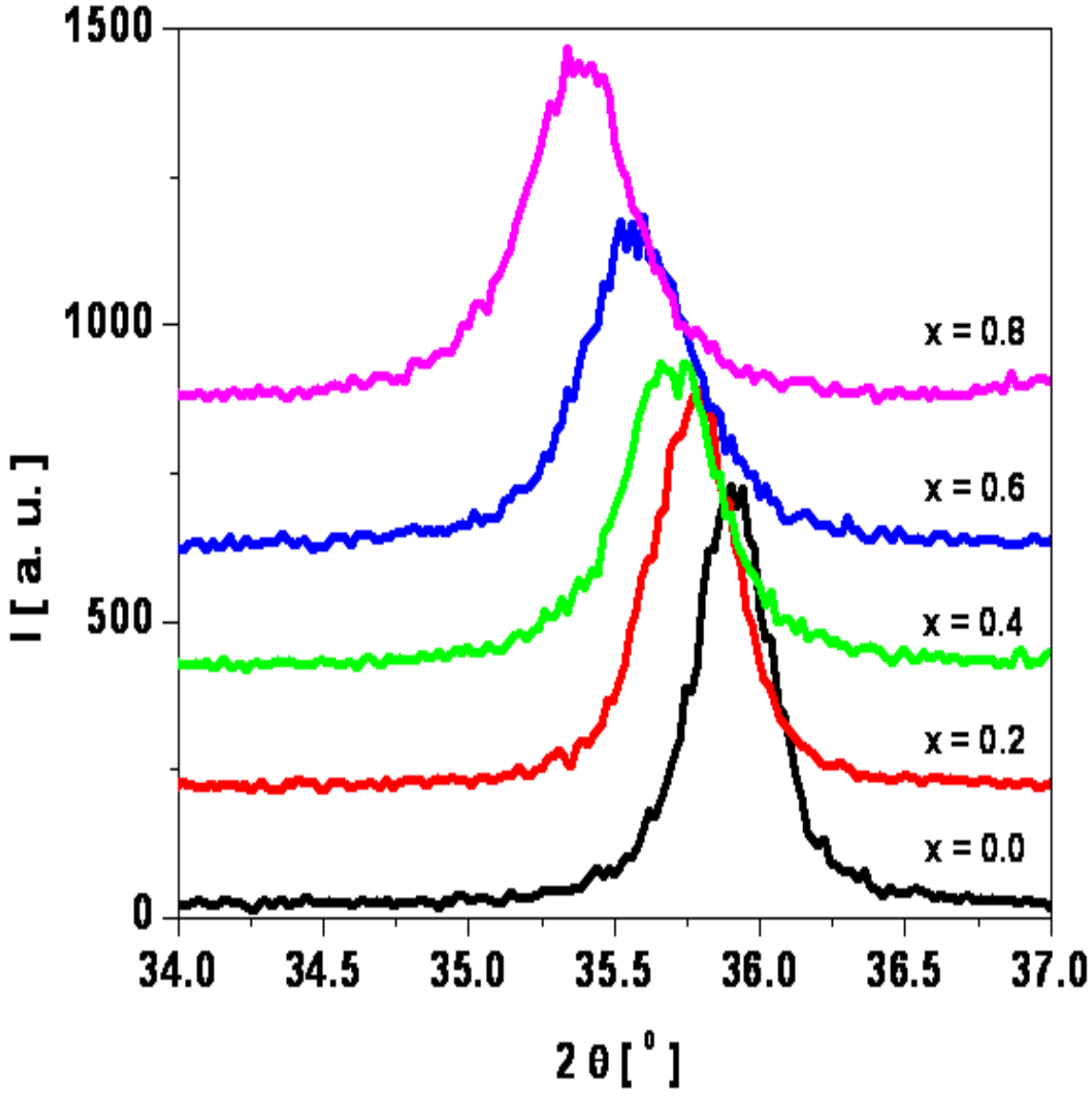

Figure 4.2: X-ray diffraction pattern of high intensity (311) peak $Ni_{1-x}Zn_xFe_2O_4$ (x = 0.0, 0.2, 0.4, 0.6, 0.8) nanoparticles.

The values for lattice constants were obtained for all the $Ni_{1-x}Zn_xFe_2O_4$ nanoparticles using the most intense (311) peak from XRD data using the equation 4.2. The values of lattice constants are listed in Table 4.1 and are plotted as shown in Figure 4.3.

$$a = d\sqrt{N} \qquad (4.2)$$

Where, *a* is lattice constant, *d* is inter planar spacing (distance between adjacent *hkl* planes - miller indices) and $N = h^2 + k^2 + l^2$.

The lattice constant *a* is observed to increases with increasing the non-magnetic Zn content *x*. This behavior of lattice constant with Zn content *x* is explained on the basis of difference in the ionic radii of Ni^{2+} and Zn^{2+}. The $Ni_{1-x}Zn_xFe_2O_4$ system has a cubic spinel configuration with unit cell consisting of eight formula units of the form $(Zn_xFe_{1-x})^A$ $[Ni_{1-x}Fe_{1+x}]^B$ O_4. The Ni^{2+} ions have a preference for the octahedral sites and Zn^{2+} ions have preference for the tetrahedral sites. The observed linear increasing of lattice constant with Zn content *x* can be attributed to the large ionic radius of Zn^{2+} (0.84 A^0) as compared to the ionic radius of Ni^{2+} (0.74 A^0). The larger ionic radii Zn^{2+} atoms replaces the smaller ionic radii Ni^{2+} atoms and thus the lattice parameters shows increasing trend with increasing non-magnetic Zn content in $NiFe_2O_4$.

Table.4.1: Particle size *D*, Lattice values *a*, X-ray density d_x of $Ni_{1-x}Zn_xFe_2O_4$ (*x* = 0.0, 0.2, 0.4, 0.6, 0.8) nanoparticles.

x	D [nm]	a [A^0]	d_x [g / cm^3]
0.0	26	8.285	5.41
0.2	23	8.311	5.39
0.4	22	8.355	5.38
0.6	19	8.415	5.36
0.8	17	8.423	5.37

The X-ray density of all the samples of the $Ni_{1-x}Zn_xFe_2O_4$ nanoferrites has been calculated from the molecular weight and the volumes of the unit cell using the equation 4.3.

$$d_x = \frac{8M}{Na^3}[g/cm^3] \qquad (4.3)$$

Where, 8 represents the number of molecules in a unit cell of spinel lattice, *M* is molecular weight, *N* is Avogadro's number and *a* is lattice parameter.

The values of X-ray density '*dx*' are given in Table 4.1. It can be seen from Table that X-ray density increases with increasing zinc content *x*. The increase in X-ray density can be related with the lattice constant.

In the present series of Ni–Zn spinel ferrites, the lattice constant increases with Zn^{2+} composition *x*. Due to increase in the lattice constant, X-ray density should have been decreased, but in the present case molecular weight increases which overtake the increase in volume of the unit cell and hence X-ray density increases with Zn content *x*.

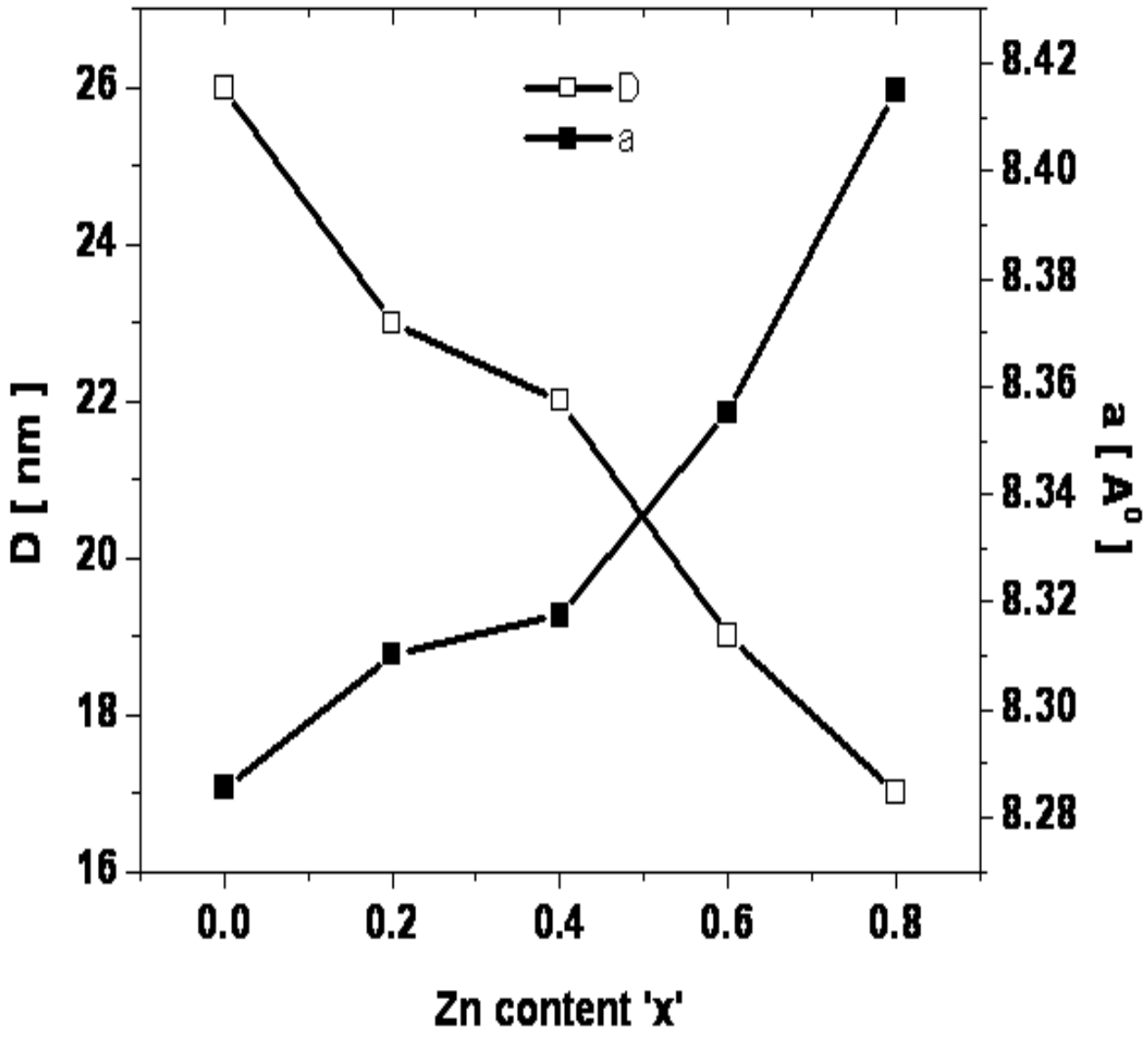

Figure 4.3: Particle size and lattice values of $Ni_{1-x}Zn_xFe_2O_4$ (*x* = 0.0, 0.2, 0.4, 0.6, and 0.8) nanoparticles.

The distance between magnetic ions at the tetrahedral A (L_A) and the octahedral B (L_B) sites was calculated using the relations (Equations (4.4) and (4.5). The variation of the hopping length L_A and L_B is also shown in Figure 4.4. Both L_A and L_B increases with Zn composition *x*. This may be attributed to the increase in lattice constant of the samples and also suggests that the jumping probability of ions is increasing.

The bond length of the tetrahedral (A) site 'd_{Ax}' (shortest distance between A-site cation and oxygen ion) and the octahedral [B] site 'd_{Bx}'(shortest distance between B-site cation and oxygen ion), the tetrahedral edge 'd_{AXE}', shared octahedral edge 'd_{BXE}' and unshared octahedral edge 'd_{BXEU}' can be calculated by putting the experimental values of lattice constant '*a*' and oxygen positional parameter '*u*' of each sample using equations 4.6 to 4.10. The values calculated from above mentioned equation are presented in Table 4. 2 indicates that the tetrahedral bond length d_{AX} and the octahedral bond length 'd_{BX}' increases as Zn content *x* increases as shown in Figure 4.5. The tetrahedral edge 'd_{AXE}', shared octahedral edge 'd_{BXE}' , unshared octahedral edge 'd_{BXEU}' does not vary much with increasing Zn content *x* as shown in Figure 4.6. This could be related to the ionic radius of Ni^{2+}, Zn^{2+} and Fe^{3+} ions.

$$L_A = \left(\frac{\sqrt{3}}{4}\right)a \qquad (4.4)$$

$$L_B = \left(\frac{\sqrt{2}}{4}\right)a \qquad (4.5)$$

$$d_{Ax} = \left(u - \frac{1}{4} \right) a\sqrt{3} \tag{4.6}$$

$$(d_{BX}) = aX\sqrt{\left(3u^2 - \frac{11}{4}u + \frac{43}{64} \right)} \tag{4.7}$$

$$d_{AE} = (2u - \frac{1}{2}) a\sqrt{2} \tag{4.8}$$

$$(d_{BE})_{shared} = (1 - 2u) a\sqrt{2} \tag{4.9}$$

$$(d_{BE})_{unshared} = aX\sqrt{\left(4u^2 - 3u + \frac{11}{16} \right)} \tag{4.10}$$

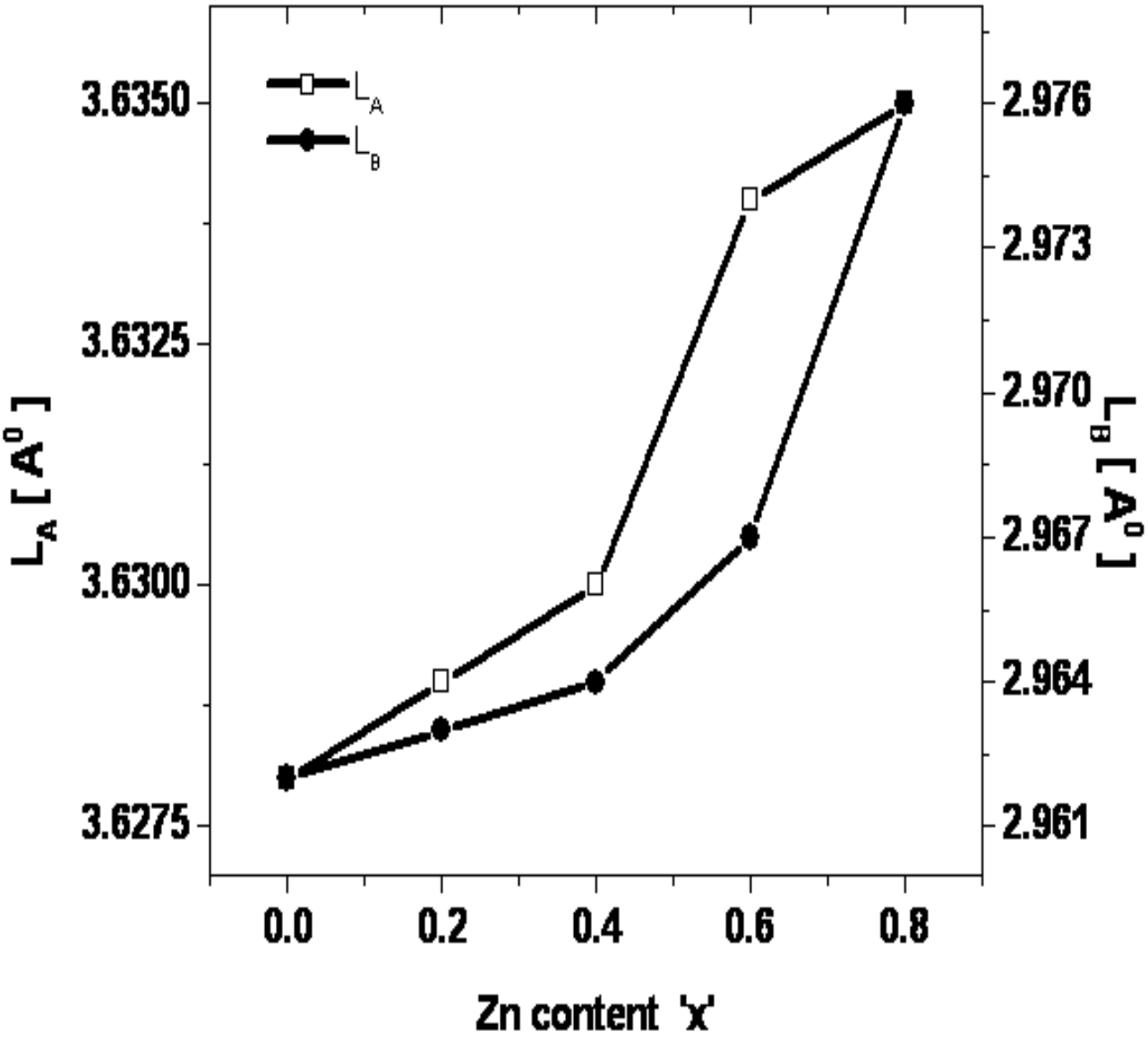

Figure 4.4: Variation of hopping length (L_A and L_B) $Ni_{1-x}Zn_xFe_2O_4$ (x = 0.0, 0.2, 0.4, 0.6, 0.8) nanoparticles.

Table 4.2: Tetrahedral bond (d_{AX}), octahedral bond (d_{BX}), tetra edge (d_{AXE}) and octa edge (d_{BXE}) (shared and unshared) of $Ni_{1-x}Zn_xFe_2O_4$ (x = 0.0, 0.2, 0.4, 0.6, 0.8) nanoparticles.

x	d_{AX} (Å)	d_{BX} (Å)	Edges		
			Tetra edge (Å)	Octa edge d_{BXE} (Å)	
			d_{AXE}	Shared	Unshared
0.0	1.880	2.025	3.069	2.788	2.937
0.2	1.886	2.031	3.079	2.797	2.946
0.4	1.887	2.033	3.081	2.799	2.948
0.6	1.896	2.042	3.095	2.812	2.962
0.8	1.909	2.057	3.117	2.832	2.983

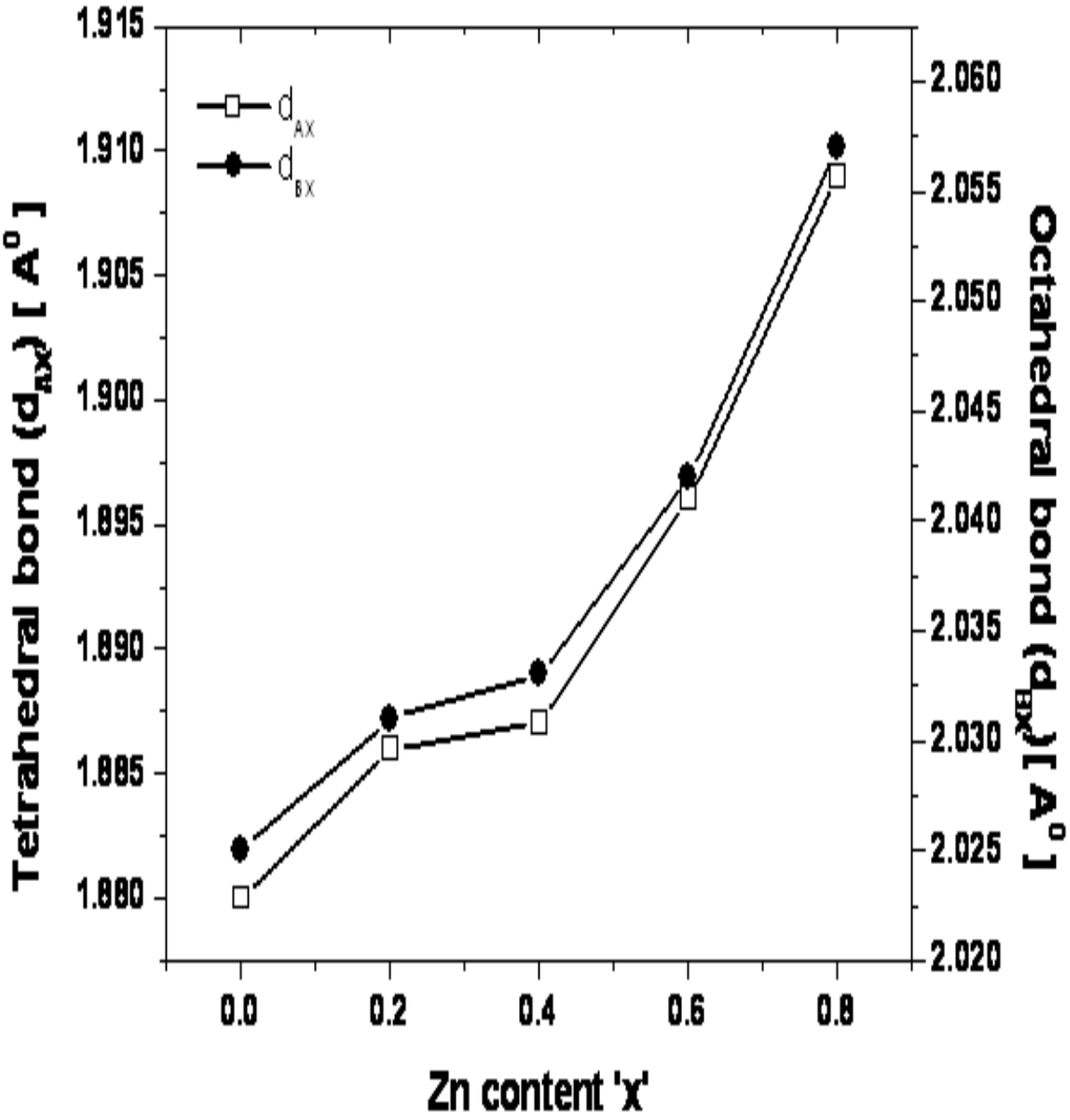

Figure 4.5: Effect of Tetrahedral bond (d_{AX}), octahedral bond (d_{BX}) on $Ni_{1-x}Zn_xFe_2O_4$ (x = 0.0, 0.2, 0.4, 0.6, 0.8) nanoparticles.

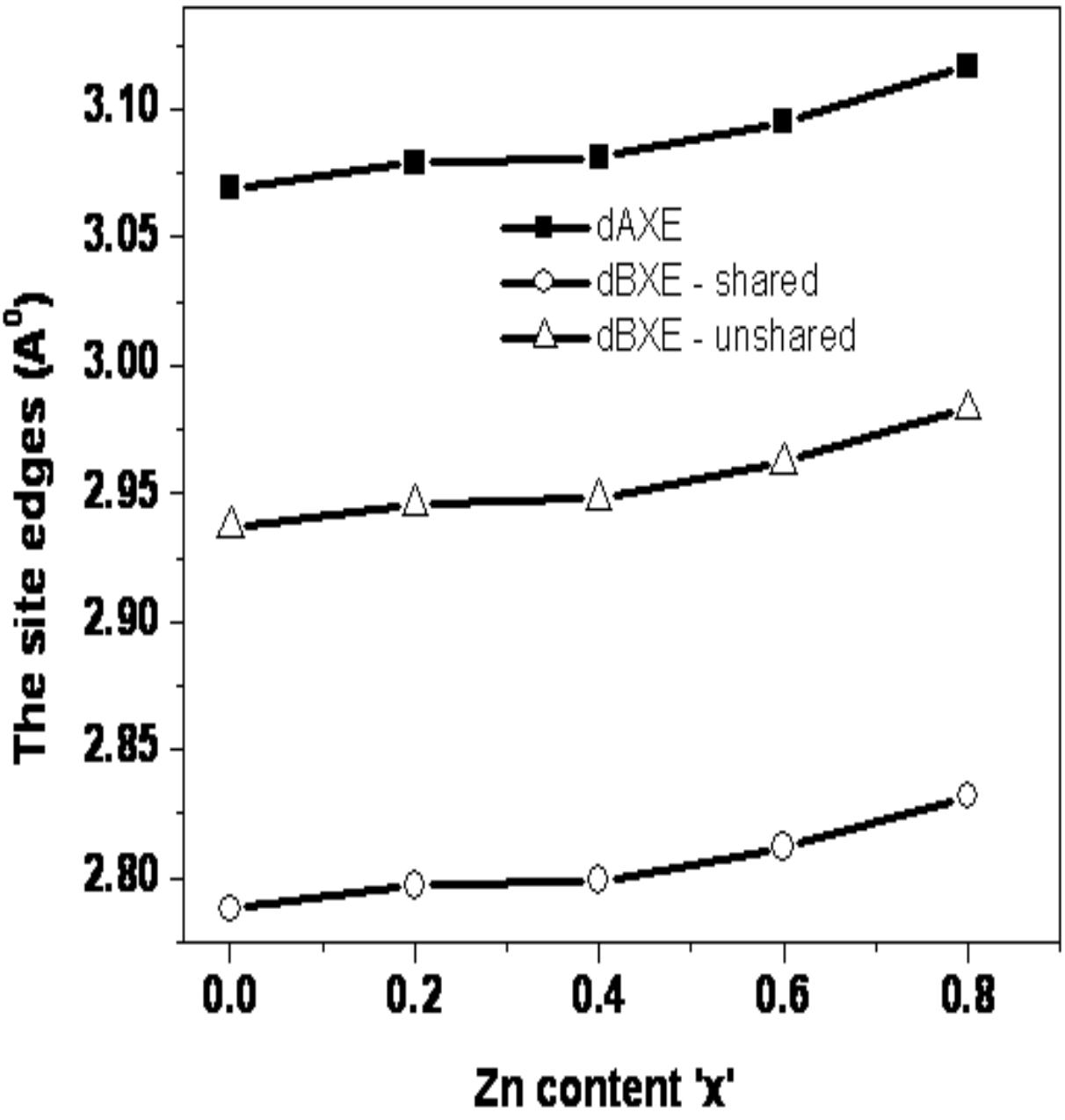

Figure 4.6: Effect of tetra edge (d_{AXE}) and octa edge (d_{BXE}) (shared and unshared) On $Ni_{1-x}Zn_xFe_2O_4$ (x = 0.0, 0.2, 0.4, 0.6, 0.8) nanoparticles.

To further support the Ni-Zn ferrite phase formation as observed from XRD data, we have carried the infrared analysis. Before any further discussion, it should be emphasized that $ZnFe_2O_4$ is normal spinel, whose structure is, according to Cotton [24], more precisely represented by formula $Zn^{2+}O$ [$Fe^{3+}{}_2O_3$], while $NiFe_2O_4$ belongs to the class of inverse spinels, whose structure is more precisely represented by formula $Fe^{3+}O$ [$Ni^{2+}Fe^{3+}O_3$], where brackets enclose the ions in the octahedral sites, and roman numbers in superscripts indicate metal atom oxidation state. This means that, during the course of preparation of samples $Ni_{1-x}Zn_xFe_2O_4$ from x = 0.0 to 0.8, one induces structural changes in both octahedral and tetrahedral units of considered samples.

Spectra of precursor samples as shown in Figure 4.7 obviously contain bands due to the vibrations of functional groups which are present in the starting chemicals. They mainly occur in the 4000 – 1000 cm^{-1} range. The absorption bands at 1350 cm^{-1} correspond to NO^{3-} ions, 1600 cm^{-1} are assigned to carboxyl (COO^-) groups and between 3150 - 3450 cm^{-1} is found a broad absorption characteristic to hydrogen-bonded OH^- groups. These bands are due to the mixed solution formed by citric acid and metal nitrates. All of these bands completely disappear by application of the high temperatures at which calcination occurs

The most interesting part of IR spectra, with respect to spinels, is in the 800 – 250 cm^{-1} range. This range is assigned to the vibrations of ions in the crystal lattice [25-29]. In this range, ferrites give rise to two most prominent absorption envelopes as shown in Fig. 4.8. Between 800 and 500 cm^{-1} v_1 band is found, which is assigned to Fe^{3+}-O and Zn^{2+}-O stretching vibrations inside the tetrahedral sites. Another absorption, v_2, is present between 450 and 300 cm^{-1}. This band is assigned to Fe^{3+}-O and Ni^{2+}-O stretching vibrations inside the octahedral sites.

The other vibrations are represented by the bands of considerably weaker intensity. The absorption peaking at 330 cm^{-1}, represented as a well resolved band for the samples $x \geq 0.4$, is assigned to ν_3, which is attributed to oscillations of zinc atoms in the isotropic force fields of their tetrahedral environment.

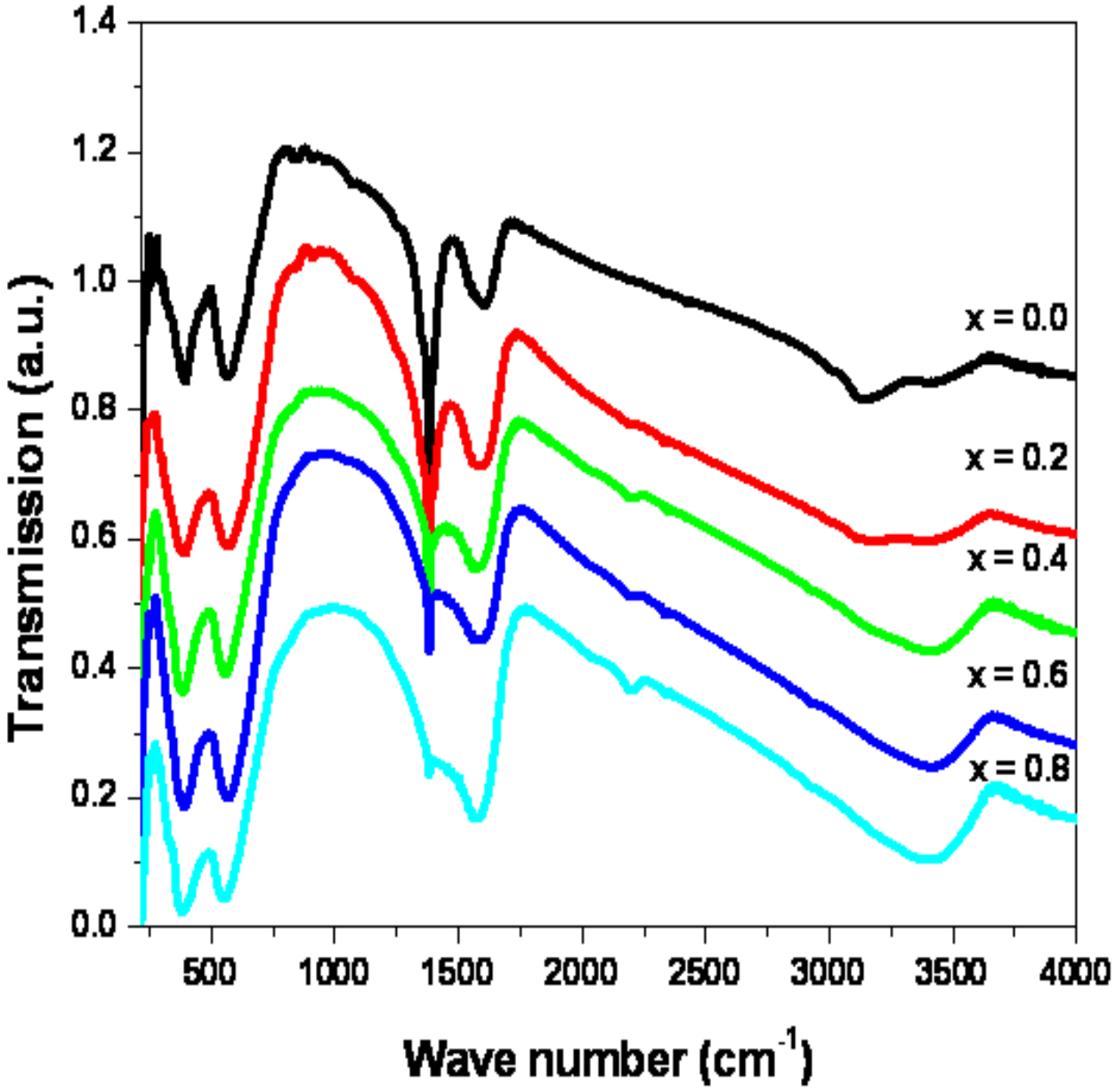

Figure 4.7: IR spectra of $Ni_{1-x}Zn_xFe_2O_4$ (x = 0.0, 0.2, 0.4, 0.6, and 0.8) precursor nano powders.

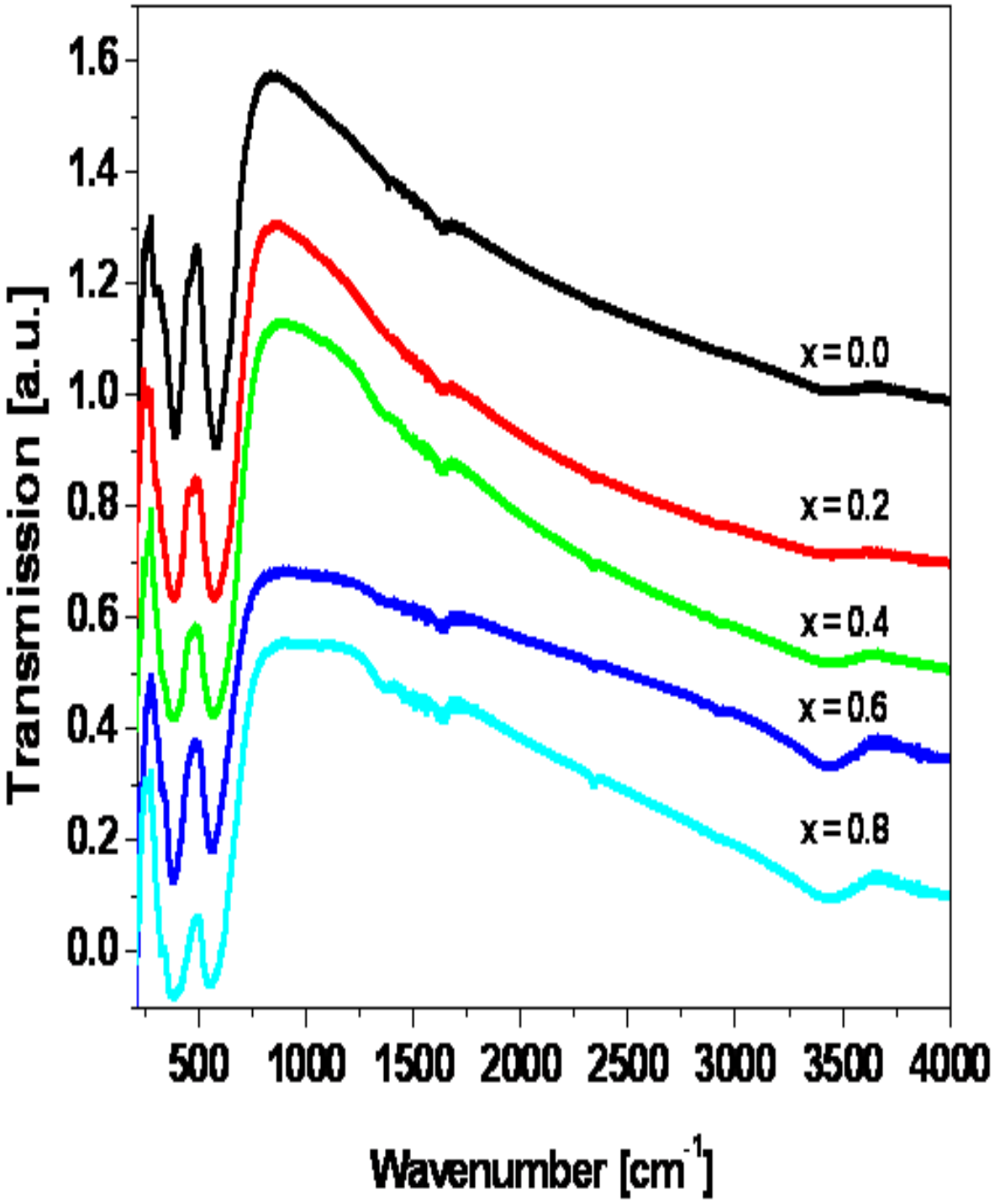

Figure 4.8: IR spectra of $Ni_{1-x}Zn_xFe_2O_4$ (x = 0.0, 0.2, 0.4, 0.6, and 0.8) nanoparticles.

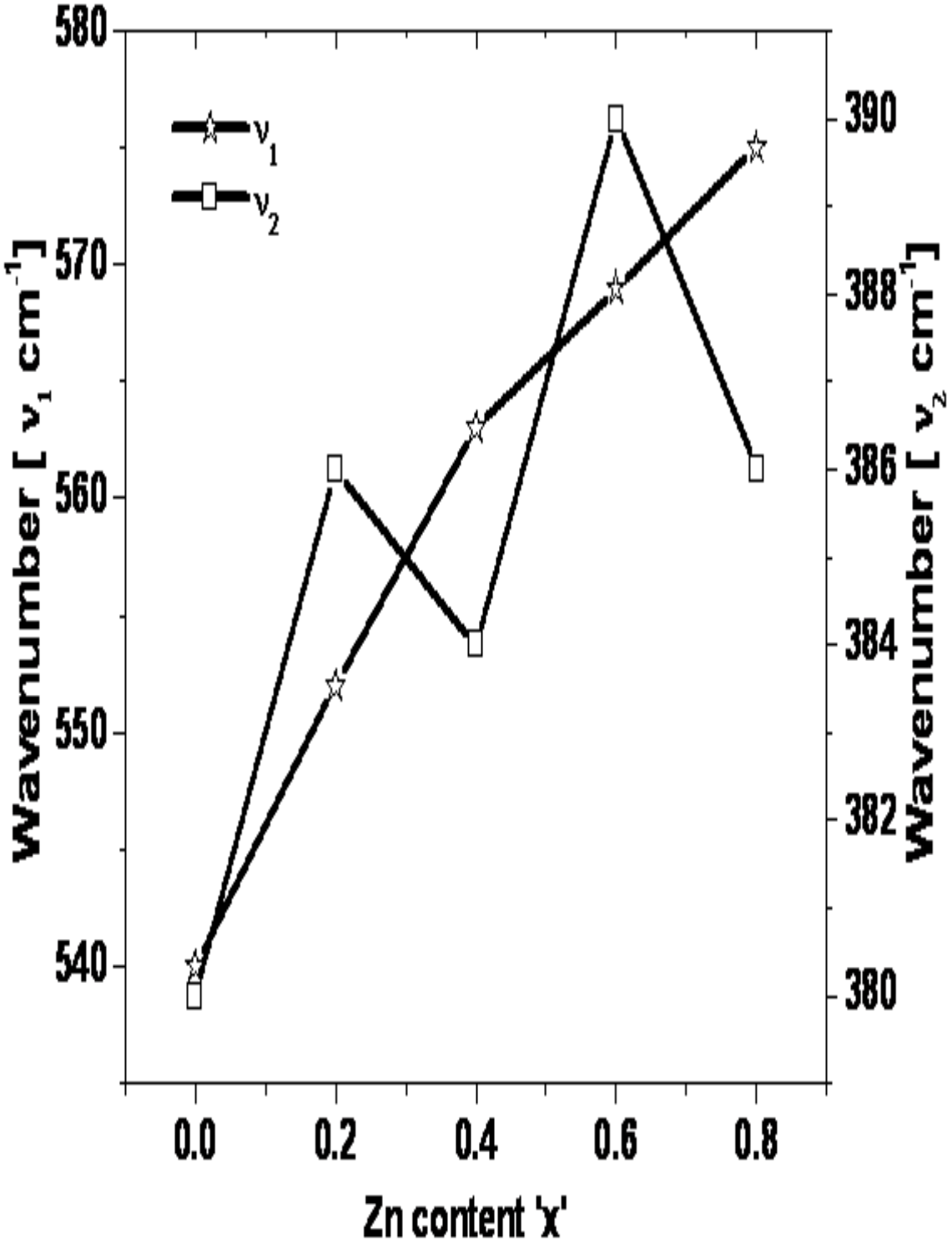

Figure 4.9: Variation of IR peak position v_1 and v_2 (cm^{-1}) for $Ni_{1-x}Zn_xFe_2O_4$ (x = 0.0, 0.2, 0.4, 0.6, and 0.8) nanoparticles.

Table 4.3: Variation of band position of ν_1 and ν_2 (cm^{-1}) for $Ni_{1-x}Zn_xFe_2O_4$ (x = 0.0, 0.2, 0.4, 0.6, 0.8) nanoparticles.

X	$\nu_1[cm^{-1}]$	$\nu_2[cm^{-1}]$
0.0	541	382
0.2	553	385
0.4	562	385
0.6	571	391
0.8	578	387

The variation of band positions υ_1 and υ_2 of $Ni_{1-x}Zn_xFe_2O_4$ with *x* is shown in Table 4.3 and Figure 4.9. Variation of ν_1 peak position for samples of different *x* prepared at corresponding calcination temperatures is more evident from Figure 4.9. Shift of this band with *x* indicates structural changes in tetrahedral sites with composition.

Although the band position and its shape are largely affected not only by chemical composition of the sample, but also by a number of other mainly uncontrollable parameters, such as conditions of synthesis etc., a general trend is clearly evident. ν_1 band shifts towards the lower wave numbers with *x* over the whole composition range. However, this shift becomes somewhat more rapid for $x \geq 0.6$, indicating weakening of the metal-oxygen bonds in the tetrahedral sites due to the transition between inverse to normal spinel structure, which is caused by increase of Zn content in the samples Zn^{2+} possesses much larger preference to tetrahedral geometry than Fe^{3+} ions. So, by increase of the Zn content (and, in turn, by decrease of nickel content) in the sample, it is expected that the transition between inverse and normal spinel structure occurs. Accordingly, the change of the slope, observed in Fig. 4.9, must be rationalized having these facts in mind. The formation of normal spinel structure due to the exchange of the positions of Fe^{3+} with Zn^{2+} ions causes weakening of the metal-oxygen bonding in tetrahedral sites.

Figure 4.10 shows SEM images of typical $Ni_{1-x}Zn_xFe_2O_4$ (x = 0.0 and 0.8) nanoparticles. As it can be seen in Figures 4.10(a) and (b), the microstructure of Ni Zn ferrite is homogeneous with equal distribution of grain sizes and porous. The microstructures of the substituted Ni Zn ferrites depicted in Figure 4.10(a) reveal a virtually uniform grain size and a homogeneous morphology. According to these micrographs, the microstructure is mainly influenced by the Zn substitution in Ni ferrite. It is observed that porosity affects the magnetic properties of the prepared nano ferrites. The pores will act as a generator of the demagnetization field. The pores obstruct the free movement of the magnetic walls during the magnetization process [30]. As a consequence, the intensity of the effective magnetic field applied to the material is reduced. Increased density reduces the material's porosity.

Therefore, a homogeneous and denser microstructure should favor the flow of the magnetic field through the material, improving its magnetic induction.

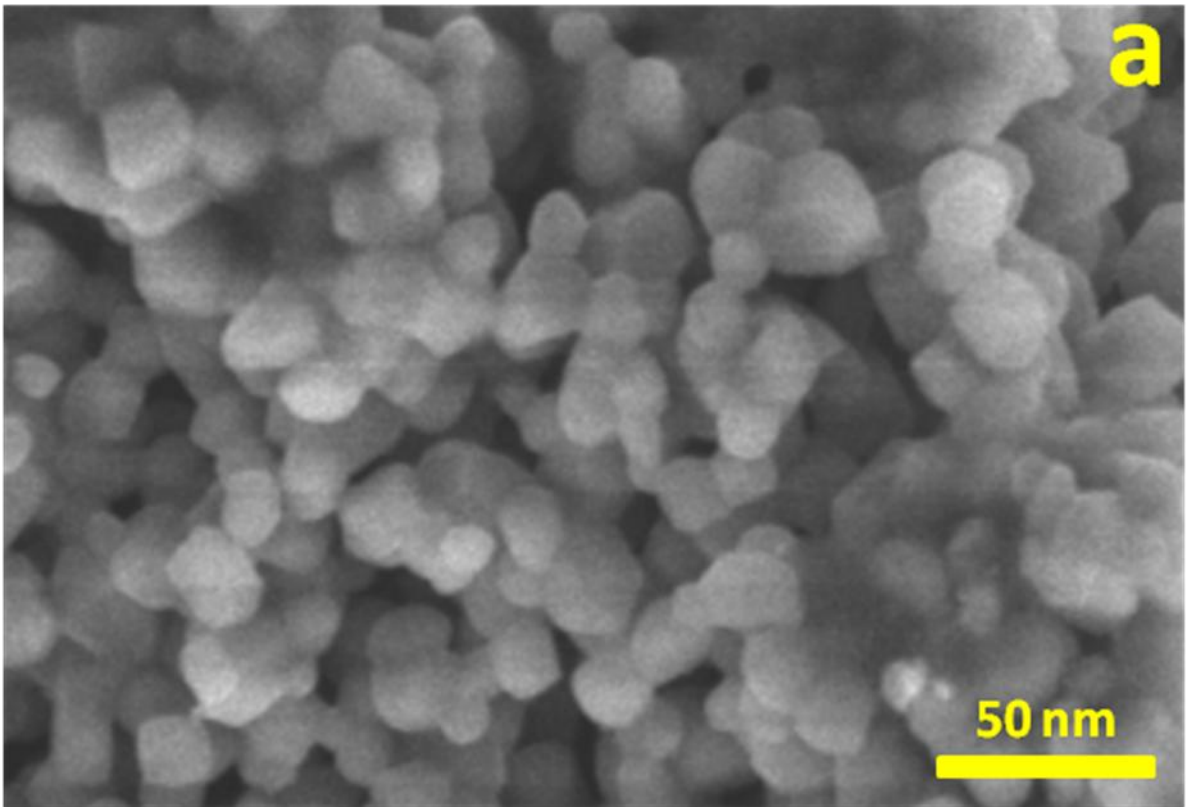

Figure 4.10(a): SEM image of $Ni_{1-x}Zn_xFe_2O_4$, x = 0.0 nanoparticles.

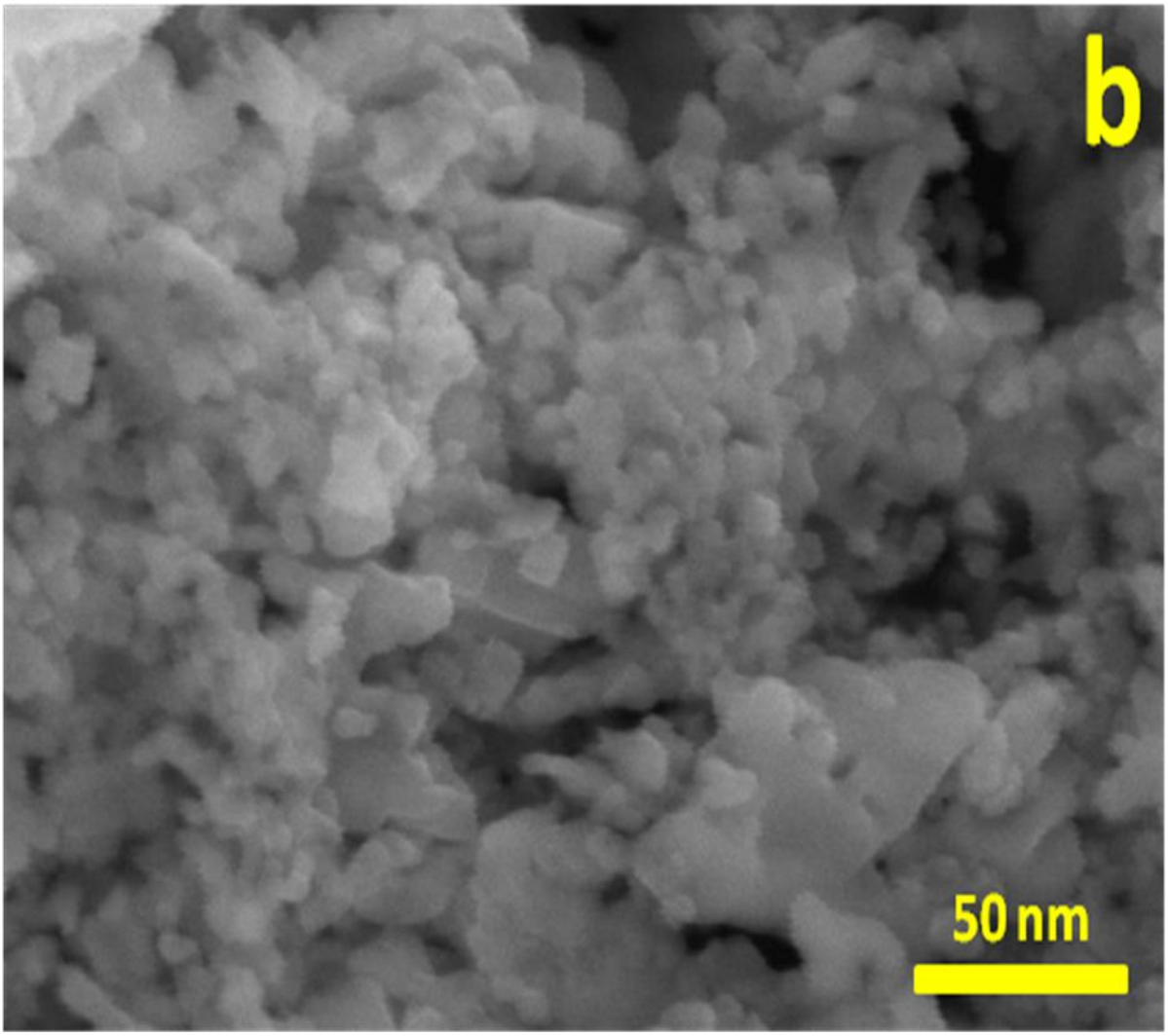

Figure 4.10 (b): SEM image of $Ni_{1-x}Zn_xFe_2O_4$, x = 0.8 nanoparticles.

4.3.2 Magnetic characterization

The hysteresis loops for the $Ni_{1-x}Zn_xFe_2O_4$ nanoparticles are as shown in Figure 4.11. The hysteresis loops does not saturate with available field of 10 kOe. The coercivity H_c reaches the value 144 Oe for x = 0.0, while the magnetization at maximum field (10 kOe) was found to be approximately 63.1 *emu/g*, much higher than the saturation magnetization 50 *emu/g* for bulk $NiFe_2O_4$ [31]. The enhanced magnetization at 10 kOe and enhanced coercivity (in comparison with the bulk material) are typical features of the canted magnetic structures as reported in Refs [32-34]. The magnetization and coercivity values were measured and plotted with different Zn concentration in Figures 4.12 and 4.13. The variation of maximum magnetization at 10 kOe does not change monotonically with the change of Zn content *x*. The values of magnetization *M* at 10 kOe, coercivity H_c and remanence M_r of various compositions of $Ni_{1-x}Zn_xFe_2O_4$ are also shown in Table 4.4. The addition of non-magnetic Zn increases the magnetic moment of the saturated samples with Zn content *x* is expected to be quite linear [35] and also weakens the exchange interactions between ions on A and B sites, which result in decreases of Curie temperature. However, with further increase of Zn content x, the magnetizations increases first and then decreases. This is due to the dilution of the spin moments which weakens the A-B interaction. That is, the average distance between interacting spins gets larger [36] and also depend upon the distribution of magnetic and non-magnetic ions at A and B sites. The magnetization value for our samples increases up to *x* = 0.4 and attains a maximum value of 63.1 emu/g and then decreases with further increase in Zn content *x*. The similar kind of behavior was observed by Goldman [37] and Yadoji et.al., [38].

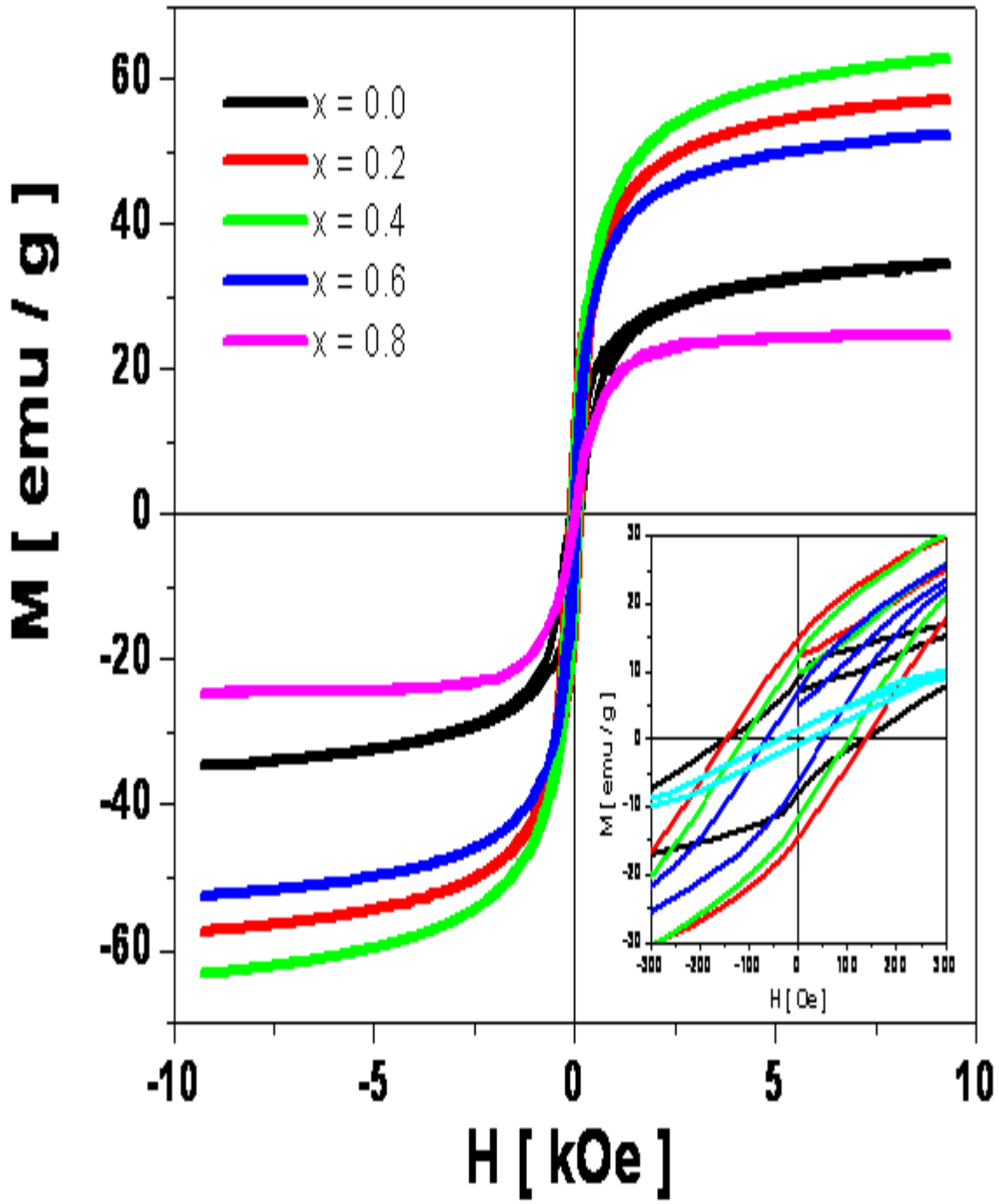

Figure 4.11: Hysteresis curves for the samples $Ni_{1-x}Zn_xFe_2O_4$ (x = 0.0, 0.2, 0.4, 0.6, and 0.8) nanoparticles

Higher Zn content *x* leads to the formation of uncoupled spins and as Zn^{2+} occupies the tetrahedral sites (site of Fe^{3+}) the spin-spin interaction between Zn^{2+} and Fe^{3+} becomes increasingly uncoupled. It is because of weakening of long range order as it is expected that high magnetic field is required to align the magnetic moment in the direction of applied field [39]. However, most types of substitutions cause a reduction of the magneto crystalline anisotropy and decrease of coercivity. With the increasing Zn content *x* the coercivity H_c is decreasing as well as particle size [Figure 4.13]. It is very well known that coercivity of nanoparticluted material is influenced by factors such as crystal structure, grain size, shape and packing density. The coercivity decreases generally with decrease in particle size, because of lower anisotropy barriers, which are in first approximation proportional to the volume (*V*) of nanoparticles [40-42]. Nanocrystalline spinel ferrites have metastable cation distributions which are found to depend on the method of synthesis and the grain size. The cation distribution changes with the grain and therefore the influence of this should be taken into account while correlating the magnetic properties. Depending on cation distribution and non-magnetic Zn content *x*, it may appear that anisotropy energy density (*K*) is reducing. This effect may also lead anisotropy barrier reduction. The change of exchange interactions between ions causes the decrease in coercivity. Therefore, the coercivity decrease in our samples may originate from change of *K* as well as V.

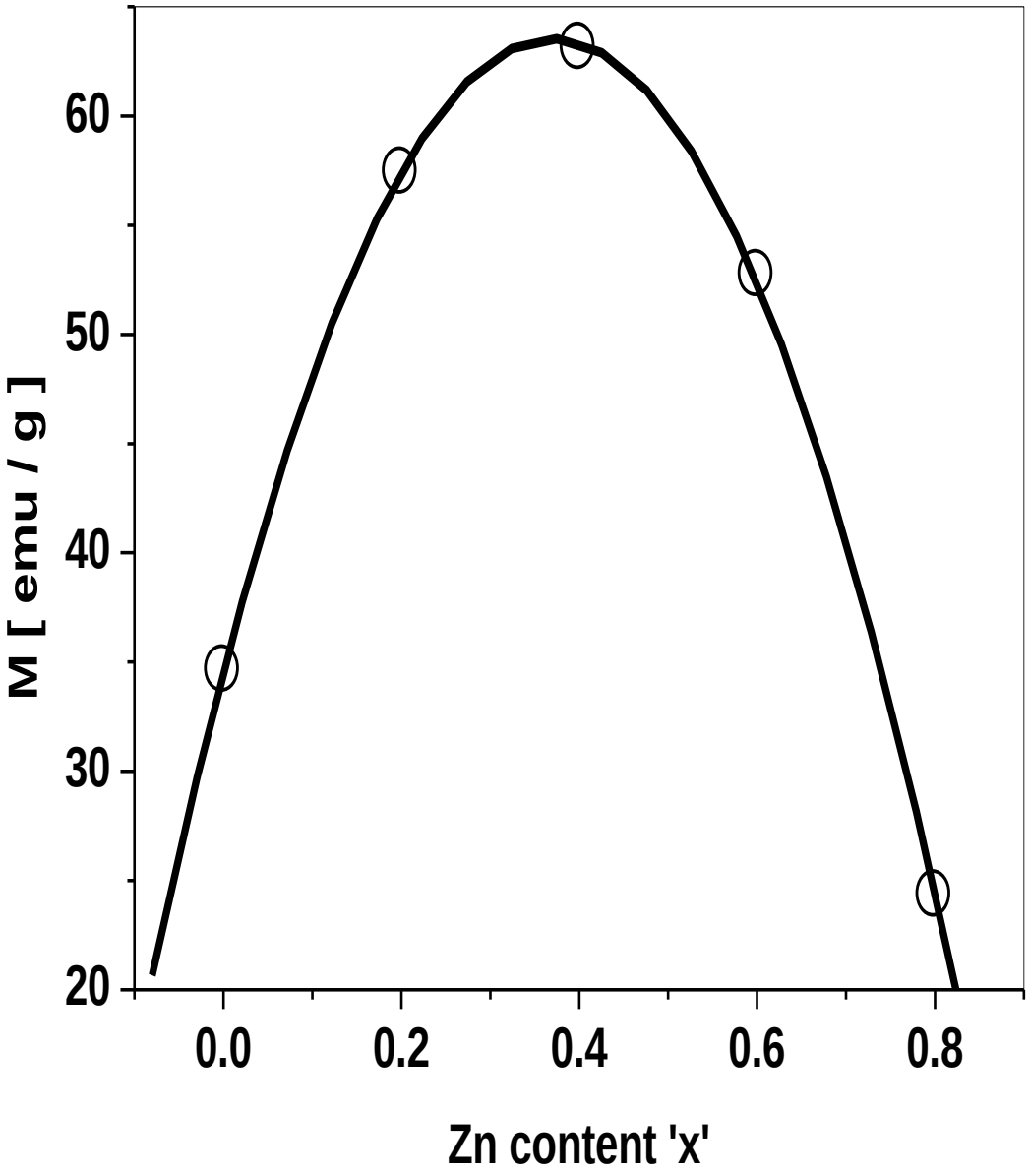

Figure 4.12: Maximum magnetization values observed for $Ni_{1-x}Zn_xFe_2O_4$ (x = 0.0, 0.2, 0.4, 0.6, and 0.8) nanoparticles from hysteresis loops (Figure 4.11).

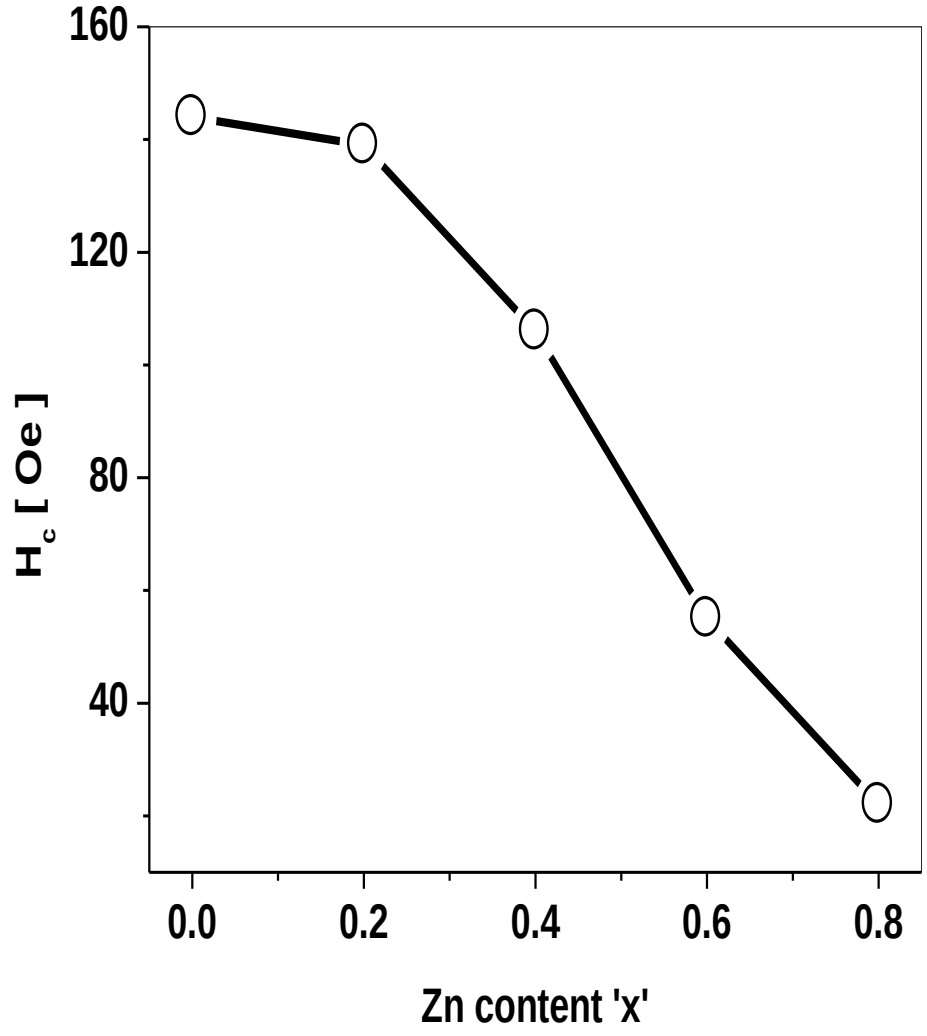

Fig. 4.13: Coercivity (H_c) values observed for $Ni_{1-x}Zn_xFe_2O_4$ (x = 0.0, 0.2, 0.4, 0.6, 0.8) nanoparticles from hysteresis loops (Figure 4.11).

Table.4.4: Coercivity H_c, remanence magnetization M_r, maximum magnetization at M, For $Ni_{1-x}Zn_xFe_2O_4$ (x = 0.0, 0.2, 0.4, 0.6, 0.8) nanoparticles observed from hysteresis loops (Fig. 4.11).

X	Hc [Oe]	Mr [emu/g]	Ms [emu/g]
0.0	144	8.52	34.6
0.2	139	14.8	57.4
0.4	106	11.9	63.1
0.6	55	6.6	52.7
0.8	22	1.4	24.3

4.4 Conclusions

1. A series of $Ni_{1-x}Zn_xFe_2O_4$ (x = 0.0, 0.2, 0.4, 0.6, 0.8) nanoparticles were prepared using oxalic acid based precursor method.

2. The XRD analysis reveals the formation of single phase spinel structure at very low annealing temperature.

3. The particle size is decreased with increasing Zn concentration.

4. The lattice parameter is increasing with increasing Zn content *x*, which is due to large ionic radii of zinc when compared to nickel.

5. The two main spectroscopic bands corresponding to lattice vibrations were observed between 200 to1000 cm^{-1}. The IR bands at 581 cm^{-1} (ν_1) and 391 cm^{-1} (ν_2) were assigned to tetrahedral (A) and octahedral [B] groups. Respectively the spectroscopic bands shift towards the lower frequencies with the increasing Zn content *x*, which reveals that substitution of zinc is taking place in the spinels.

6. Magnetic measurements at room temperature for these samples revealed that magnetization at ≈1*T* do not change monotonically with the change of Zn content *x*.

7. The coercivity and remanence decreases with increasing non-magnetic Zn content *x*.

All of this could originate from reduced exchange interactions and decreased nanocrystallite size with increasing Zn content *x*.

4.5 References

[1] Z. Zhong , Q. Li, Y. Zhang, H. Zhong, M. Cheng, Y. Zhang, Powder Technology. 155 (2005) 193-195.

[2] Z. Yue, J. Zhou, L. Li, H. Zhang, Z. Gui, J. Magn. Magn. Mater. 208 (2000) 55-60.

[3] X. He, G. Song, J. Zhu, Materials Letters. 59 (2005) 1941-1944.

[4] Y. Matsuo, M. Inagaki, T. Tomozawa, F. Nakao, IEEE Trans. Magn. 37 (2001) 2359-2361.

[5] P.S. Anil Kumar, J.J. Shrotri, S.D. Kulkarni, C.E. Deshpande, S.K.Date, Mater. Lett. 27 (1996) 293-296.

[6] H. Su, H. Zhang, X. Tang, Y. Jing, Y. Liu, J. Magn. Magn. Mater. 310 (2007) 17-21.

[7] J.L. Dormann, M. Nogues, J. Phys.: Condens. Matter. 2 (1990) 1223-1237.

[8] N. Rezlescu, E. Rezlescu, C. Pasnicu, M.L. Craus, J. Phys. Condens. Matter. 6 (1994) 5707-5716.

[9] A.E. Virden, K. O'Grady, J.Magn.Magn.Mater. 290–291 (2005) 868-870.

[10] A.M. El-Sayed, Ceramics. Int. 28 (2002) 363-367.

[11] A. Dias, R.L. Moreira, Materials Letters. 39 (1999) 69-76.

[12] S. E. Jacobo, S. Duhalde, H.R. Bertorello, J. Magn. Magn. Mater. 272–276 (2004) 2253-2254.

[13] S.D. Shenoy, P.A. Joy, M.R. Anantharaman, J. Magn. Magn. Mater. 269 (2004) 217-226.

[14] S. A. Morrison, C. L. Cahill, E. E. Carpenter, S. Calvin, R. Swaminathan, M. E. McHenry, V. G. Harris, J.Appl.Phys. **95** (2004) 6392-6395.

[15] J. Sun, J. Li, G. Sun, W. Qu, Ceramics International. 28 (2002) 855-858.

[16] A. Verma, T.C. Goel, R.G. Mendiratta, M.I. Alam. Mat. Sci. Engg. B60 (1999) 156-162.

[17] S. Yan, J. Yin, E. Zhou. Colloids and Surfaces A: Physicochem. Eng. Aspects. 287 (2006) 153-157.

[18] G. Pozo Lopez, S.P. Silvetti, S.E. Urreta, E.D. Cabanillas. Physica B. 398 (2007) 241-244.

[19] C. Upadhyay, D. Mishra, H.C. Verma, S. Anand, R.P. Das. J. Magn. Magn. Mater. 260 (2003) 188-194.

[20] D.G. Wickham, Inorg. Synth. 9 (1967) 152.

[21] A. T. Raghavender, S. E. Shirsath, K. Vijaya Kumar, J. Alloys. Comp. 509 (2011) 7004.

[22] A.T. Raghavender, D. Pajic, K. Zadro, T. Milekovic, P. Venkateshwar Rao, K.M. Jadhav, D. Ravinder, J. Magn. Magn. Mater. 316 (2007) 1.

[23] E. Auzans, D. Zins, E. Blums, R. Massart, J. Mater. Sci. 34 (1999) 1253.

[24] F. A. Cotton, G. Wilkinson, Advanced Inorganic Chemistry, 5^{th} edition, John Willey and Sons, New York, 1988, page 9.

[25] R.D. Waldron, Phys. Rev. 99 (1955) 1727-1735.

[26] E.Auzans, D.Zins, E.Blums, R.Massart, J.Mater.Sci. 34 (1999) 1253-1260.

[27] Z. Yue, W. Guo, J. Zhou, Z. Gui, L. Li, J. Magn. Magn. Mater, 270 (2004) 216-223.

[28] M.Andres – Verges, C. De Julian, J.M. Gonsalez, C.J.Serna, J.Mater.Sci. 28 (1993) 2962-2966.

[29] C. Prakash, J.S. Baijal, Solid. State. Commun. 50 (1984) 557-559.

[30] A. R. Bueno, M. L. Gregori , M. C.S. N´obrega, Mate.Chem.Phys. 105 (2007) 229-233.

[31] M.U. Rana, T. Abbas, F.A. Khawaja, Mater. Lett. 52 (2002) 389-393.

[32] V.Sepelak, D. Baabe, D. Mienert, D. Schultze, F. Krumeich, F.J. Litterst, K.D. Becker, J. Magn. Magn. Mater. 257 (2003) 377-386.

[33] R.H. Kodama, A.E. Berkowitz, E.J. McNiff, S. Foner, Phys. Rev. Lett. **77** (1996) 394-397.

[34] R.H. Kodama, A.E. Berkowitz, Phys. Rev. B. 59 (1999) 6321-6336.

[35] B.D.Cullity, C.D.Graham, Introduction to magnetic materials, John Wiley and Sons Publications, Canada, 2009.

[36] J. Smit, H.P.J. Wijn, "Ferrites" Physical Properties of Ferrimagnetic Oxides in Relation to Their Technical Applications, Phillips, Eindhoven, 1959, p. 149.

[37] A. Goldman, Modern Ferrite Technology, Second Edition, Springer, U.S.A., 2006.

[38] P. Yadoji, R. Peelamedu, D. Agrawal , R. Roy, Mate. Sci. Engg. B. 98 (2003) 269-278.

[39] T.T. Srinivasan, P. Ravindranathan, L.E. Cross, R. Roy, R.E.Newnham, S.G. Sankar, K.C. Patil, J. Appl. Phys. 63 (1988) 3789-3791.

[40] C.P. Bean, J.D. Livingston, J. Appl. Phys. 30 (1959) S120-129.

[41] E.C. Stoner, E.P. Wohlfarth, Philos. Trans. R. Soc. Lond. A 240 (1948) 599 - 642 reprinted in IEEE Trans. Magn. 27 (1991) 3475-3518.

[42] L. Yu, J. Zhang, Y. Liu, C. Jing, S. Cao, J. Magn. Magn. Mater. 288 (2005) 54-59